Nonhydrostatic haline convection under leads in sea ice

David C. Smith IV

Environmental Fluid Dynamics Program, Mechanical and Aerospace Engineering Department Arizona State University, Tempe

James H. Morison

Polar Science Center, Applied Physics Laboratory, University of Washington, Seattle

Abstract. The distribution of dense brine under leads in sea ice is associated with convective sinking of individual plumes and near-surface mixing associated with ice-water momentum flux. The processes have been studied in the recent Lead Experiment (LeadEx) field program and previously modeled using a two-dimensional hydrostatic numerical model. In this study these processes are reexamined using a nonhydrostatic model. It is shown that nonhydrostatic effects give rise to pressure distributions which counter hydrostatic pressure gradients in the fluid. These effects are largest in sinking plume events and can be substantial when plumes are free to sink to depths of 100 m. In the presence of the Arctic halocline (typically at 30-40 m), however, vertical accelerations of convective plumes are limited spatially and temporally, and nonhydrostatic effects are relatively small. It is the purpose of this paper to demonstrate that for realistic Arctic stratification, convective circulations under leads in sea ice are predominantly hydrostatic.

1. Introduction

Leads are small-scale (<1 km wide) cracks in sea ice in the Arctic ice pack. They occur in response to the mechanical action of wind stress on the ice pack and stress within the ice. Leads occupy a relatively small percentage of the areal extent of ice (only several percent). Despite their small size and relatively limited areal extent, however, they are important windows in the pack ice where heat exchange processes occur. Convective processes occur in both the atmosphere and ocean near leads. In the atmosphere, convection is driven by oceanic heat loss to the air. Upper ocean heat losses result in the formation of new ice in the lead. Brine rejection associated with new ice formation leads to convection processes beneath the lead in the upper water column. Observations of these processes have been made in the recent field program, Lead Experiment (LeadEx). Prior knowledge of these processes has been summarized by Morison et al. [1992]. Observations of lead convection taken during LeadEx are described by Morison and McPhee [this issue] and McPhee [this issue].

Numerical studies of oceanic convection under leads have been conducted by Kozo [1983], Smith and Morison [1993], and Kantha [1995]. These prior model studies were performed with hydrostatic ocean models. In this study the convective circulations in the upper ocean associated with leads in sea ice are studied with a nonhydrostatic ocean model. We will illustrate differences between hydrostatic and nonhydrostatic runs by examining deviations from hydrostatic pressure in nonhydrostatic model runs. We will show that nonhydrostatic convective circulation cells are weaker than corresponding hydrostatic ones but that the circulation cells have a remarkably similar qualitative appearance.

We will also examine the importance of the halocline in limiting haline convection beneath leads. The introduction of a

Copyright 1998 by the American Geophysical Union.

Paper number 97JC02262. 0148-0227/98/97JC-02262\$09.00 halocline under the lead reduces the role of planetary rotation in the convective flow. Using a hydrostatic model, Smith and Morison [1993] argue that convective plumes would penetrate to several thousand meters depth in the Arctic in the absence of the halocline at 40–60 m. At this depth the plume penetration would be limited by rotational adjustment as discussed by Maxworthy and Narimousa [1994] and Jones and Marshall [1993]. Hence the presence of the halocline limits the role that rotation plays. We will find here that the halocline also limits nonhydrostatic effects.

The ability of convective plumes to penetrate a density interface has been examined by S. Narimousa and T. Maxworthy (unpublished manuscript, 1994) and by Fernando and Ching [1993a, b]. In these studies, laboratory experiments are used to determine stability criteria which must be met for plumes to penetrate a density interface. Important parameters in this process are the buoyancy flux at the surface, the depth of the convective layer, and the buoyancy of the interface. For typical Arctic parameters they estimate that plumes are unable to penetrate the halocline stratification and instead should spread laterally in the mixed layer as a gravity current, across the upper halocline. As discussed below, our results are in agreement with this assessment.

The redistribution of salt beneath leads is associated with convective sinking and turbulent mixing in the boundary layer. The relative importance of these two factors is dependent on the ice-water relative motion and can be quantified in terms of a lead number. *Morison et al.* [1992] define the lead number in terms of the ratio of the pressure gradient term to the turbulent stress term in the lateral momentum equation. When the lead number is less than order 1, convective processes dominate in the mixing of salt. For lead numbers greater than order 1, mechanical ice-water stress-induced mixing redistributes the salt. Both processes are important for lead number O(1), which occurs for relative ice-water speeds around 7 cm s⁻¹ for typical lead conditions. The model study by *Smith and Morison* [1993] illustrates the salt distributions for a range of lead num-

(1)

bers and found good agreement with the observations discussed by *Morison et al.* [1992]. This study differs from that by *Smith and Morison* [1993] in several ways. In that study a hydrostatic model was used, and emphasis was on circulations associated with both free convection (low lead number) and forced convection (high lead number) cases. Here we seek to illustrate nonhydrostatic effects and thus will be emphasizing the low lead number regime where nonhydrostatic effects should be most important. The paper is organized as follows. Section 2 describes the nonhydrostatic numerical model. Results are described in section 3. A comparison with previous theory is given in section 4, followed by conclusions.

2. Model Description

In this study we use a nonhydrostatic, Boussinesq, rotating, two-dimensional model. The momentum and continuity equations are

$$\frac{\partial u}{\partial t} + u \frac{\partial u}{\partial x} + w \frac{\partial u}{\partial z} + \frac{1}{\rho_o} \frac{\partial p'}{\partial x} - fv =$$

$$-B_H \nabla^4 u - k_m \frac{\partial^2 u}{\partial z^2} + \tau_{iw}$$

$$\frac{\partial v}{\partial t} + u \frac{\partial v}{\partial x} + w \frac{\partial v}{\partial z} + fu = -B_H \nabla^4 v - k_m \frac{\partial^2 v}{\partial z^2}$$
 (2)

$$\frac{\partial w}{\partial t} + u \frac{\partial w}{\partial x} + w \frac{\partial w}{\partial z} + \frac{1}{\rho_0} \rho' g + \frac{1}{\rho_0} \frac{\partial p'}{\partial z} = -B_H \nabla^4 w \tag{3}$$

$$\frac{\partial u}{\partial x} + \frac{\partial w}{\partial z} = 0 \tag{4}$$

for velocity components u, v, and w. Other model notation and parameter values are contained in the notation section. The equations are finite differenced on a c grid with vertical resolution $2\Delta z = 5$ m and horizontal resolution $2\Delta x = 10$ m. The model domain is 100 m deep and 750 m wide. A study of Rayleigh-Benard convection in gridded systems by Xu and Lin [1993] provides some guidance on how to select vertical resolution. Their study indicates that the model must resolve the fastest growing vertical wave mode with at least 10 points. Models with fewer points in the vertical do not resolve the fastest growing wave. This criterion is met with the choices of depth and resolution here. The fastest growing wave in our experiments has a horizontal wavelength of O(100 m). We have also done simulations with higher resolution than 10 m and found that this wavelength does not change, indicating that we have adequately resolved the instability process.

Lead width is fixed at 250 m in all experiments. Sensitivity of model results to varying lead width is considered by *Smith and Morison* [1993].

Although the equations include planetary rotation, the effects of rotation on the convection in these experiments are limited. As is illustrated by Smith and Morison [1993], rotation produces along-lead jets normal to the x-z plane of the model. See Smith and Morison [1993] for a discussion of the magnitude and distribution of these jets. Rotation does not, however, play the role that it does in deeper convection studies. The studies of Jones and Marshall [1993], Maxworthy and Narimousa [1994], and Fernando et al. [1991] have illustrated that rotation can limit the depth of penetration of convective plumes. A critical depth $z_c = (q_0/f^3)^{1/2}$ defined in terms of

buoyancy flux q_0 and Coriolis parameter f is found to be the depth that plumes penetrate in a homogeneous rotating fluid. For parameters in this study, z_c is O(5000 m), indicating that rotation does not play a role in arresting plume descent in this shallow convection study. In three-dimensional laboratory experiments the subsequent evolution of these geostophic jets can be dominated by baroclinic instability. Fernando and Ching [1993b], for example, report that these instabilities break the jets into eddies after the plume impinges on the density interface. They note that a typical timescale of six inertial periods is required for this instability to occur, i.e., timescales longer than those considered here.

As a measure of nonhydrostatic pressure, we take the ratio of nonhydrostatic terms on the left-hand side of (3) to the vertical pressure gradient

$$NH_{\Sigma} = \frac{\frac{\partial w}{\partial t} + u \frac{\partial w}{\partial x} + w \frac{\partial w}{\partial z}}{\frac{1}{\rho_{c}} \frac{\partial p'}{\partial z}}$$
(5)

In subsequent discussion we will refer to this ratio as NH_{Σ} . We will examine time dependence and spatial distributions of this term to illustrate nonhydrostatic effects.

The role of nonhydrostatic terms in atmospheric convection has been examined by Yang [1991]. In the context of a sea breeze model, Yang showed that lateral pressure gradients in a nonhydrostatic model are countered by pressure gradients associated with the nonhydrostatic terms. The result is to weaken the convection cells in a nonhydrostatic model relative to that in a hydrostatic code. However, Yang also concluded that these effects are small and are only important in strongly forced sea breeze cells and then only near the source of the buoyancy flux. In a manner analogous to that used by Yang [1991] we will examine these pressure effects in the context of shallow oceanic convection under leads in sea ice.

Advection and diffusion of salt is governed by

$$\frac{\partial S}{\partial t} + u \frac{\partial S}{\partial x} + w \frac{\partial S}{\partial z} = \frac{\partial}{\partial z} k_S \frac{\partial S}{\partial z} - B_S \nabla^4 S + Q_S \qquad (6)$$

for salinity, S (g kg⁻¹).

 Q_S is a salt flux source term.

$$Q_{S} = \frac{w'S'}{\lambda_{s}} \exp\left(\frac{-z}{\lambda_{s}}\right) \tag{7}$$

The term λ_r is an e-folding scale (=2 m) over which salt is distributed at the top of the model domain. This distributed source of salt crudely represents sub-grid-scale processes such as frazil ice formation that are not included in the model. The salt flux w'S' is specified to be = 2×10^{-5} m g kg⁻¹ s⁻¹ and is taken from lead observations reported by *Morison and McPhee* [this issue].

As in the previous study [Smith and Morison, 1993], sub-grid-scale vertical mixing (k_m, k_s) is represented by the scheme of Pacanowski and Philander [1981]. The amount of turbulent dissipation is an important consideration for this model. The real difficulty is separation of the turbulence from the motions we wish to simulate. The dominant wavelengths of turbulent eddies in the boundary layer with no horizontal inhomogeneity are of the order of the mixed layer depth. The horizontal inhomogeneities in the flow field caused by the lead and convection in the lead are of a similar size. To simulate these



disturbances, we have avoided explicitly fixing the eddy coefficient at a level as high as one would expect in a horizontally uniform, convective boundary layer driven by the salt flux under the lead. Instead, we have invoked the eddy coefficient of Pacanowski and Philander [1981] for sub-grid-scale closure. The Richardson number dependence in the Pacanowski and Philander scheme allows for some simple dependence of mixing on stratification, without attempting to parameterize convective mixing at the scales of lead driven circulation. The coefficients k_m and k_s are limited to range from small positive values $(1 \times 10^{-4}, 1 \times 10^{-5} \text{ m}^2 \text{ s}^{-1})$ to 0.01 m² s⁻¹. With the addition of a limiting value of ku_*z , effective in the top few meters, this produces surface velocities in the forced convection experiments consistent with observed drag laws. The plumes resolved in the simulations of active leads increase the total effective mixing above that due to the sub-grid-scale closure. The role that sub-grid-scale mixing plays in convection from line segment sources is also considered by Lavelle and Smith [1996]. In that study a three-dimensional numerical model with a Smagorinsky [1963] mixing scheme is contrasted with comparable laboratory experiments of Fernando and Ching [1993a]. While that study illustrates the utility of the Smagorinsky mixing scheme in getting agreement with laboratory data, we have not included that mixing scheme in this study. The study of Kantha [1995] also considers the sub-grid-scale mixing issue. In that study, Mellor and Yamada [1982] turbulence closure is incorporated.

We have found that the *Pacanowski and Philander* [1981] scheme does not provide enough damping to maintain numerical stability. We have thus applied a biharmonic smoother in both x and z directions to all components of the velocity field to damp grid-scale motion. This operator is also applied to the salinity field. The biharmonic coefficients B_H and B_S are chosen as the minimum values possible for numerical stability. As is discussed below, however, the biharmonic damping and dissipation terms are important factors in controlling the convective events in these simulations.

At temperatures near the freezing point, density variations are more dependent on salinity than temperature. We thus retain a simple equation of state for density (kg m⁻³)

$$\rho = 0.808 \, (kg^2 \, m^{-3} \, g^{-1}) S + 1000 \tag{8}$$

which is a function of salinity (g kg^{-1}) only [Morison, 1980].

In contrast to the previous study, the vertical momentum equation is nonhydrostatic. This necessitates solving for the pressure field in a manner described by *Brugge et al.* [1991]. The pressure field is obtained by taking the divergence of the momentum equations (1)–(3) and utilizing the continuity equation (4). This results in an elliptic equation for pressure

$$\frac{\partial^2 p'}{\partial x^2} + \frac{\partial^2 p'}{\partial z^2} = \frac{\partial}{\partial x} RHS_x + \frac{\partial}{\partial z} RHS_z$$
 (9)

where

$$RHS_{x} = \rho_{0} \left(-\frac{\partial u^{2}}{\partial x} - \frac{\partial uw}{\partial z} + fv - B_{H} \nabla^{4} u - k_{m} \frac{\partial^{2} u}{\partial z^{2}} + \tau_{iw} \right)$$
(10)

$$RHS_z = \rho_0 \left(-\frac{\partial uw}{\partial x} - \frac{\partial w^2}{\partial z} - \frac{g\rho'}{\rho_0} - B_H \nabla^4 w \right)$$
 (11)

This is solved in the present study using a direct solver [Swarztrauber and Sweet, 1975] subject to rigid top and bottom boundary conditions

$$w = 0$$
 $z = 0, -H$ (12a)

and

$$\frac{\partial p'}{\partial z} = -\rho' g \qquad z = 0, -H \tag{12b}$$

Lateral boundary conditions are periodic.

3. Results

3.1. Homogeneous Case

The convective process is illustrated first for an initially homogeneous layer with a depth of 100 m. It might represent conditions over a well mixed shelf region near the end of winter. Plate 1 shows velocity vectors and salinity field at four times (t = 1.5, 3, 4.5, and 6 hours) during the first inertial period. As in work by Smith and Morison [1993], the release of buoyantly unstable plumes occurs first at lead edges with subsequent migration toward the lead center. Observations taken during the LeadEx experiment also indicate that plumes are released predominantly near the ice edges of the leads [Morison and McPhee, this issue]. By taking the curl of the momentum equations (1) and (3) one can see that along-lead vorticity $\zeta_{\rm w}$ is generated by lateral gradients in density. For a salt source which is uniform within the lead these gradients are largest at lead edges, producing $+\zeta_{\nu}$ on the left boundary and $-\zeta_{\nu}$ on the right lead edge. Maps of model ζ_y are presented by Smith and Morison [1993] to confirm these vorticity arguments. Maximum vertical velocities reach 0.08 m s⁻¹ during plume events in experiment 1. These are also times when nonhydrostatic effects reach local maximum values. The time dependent release and spacing of the plumes is discussed below and is compared with previous theory and laboratory results.

The degree of departure from the hydrostatic balance for the strongest plume event (t=4.5 hours) in experiment 1 is illustrated in Plate 2a. Plate 2 shows spatial distribution of the ratio (NH_{Σ} , (5)) of the first three terms on the left-hand side of (3) to the root-mean-square (rms) value of the vertical pressure gradient. Plate 2 illustrates that nonhydrostatic terms can be of the same magnitude as the hydrostatic term and hence are an important contributor to the vertical dynamical balance in the absence of stratification. Maximum values of NH_{Σ} are O(1) and occur along the axes of descending plumes. Further discussion of the distributions of minimum and maximum values of NH_{Σ} is given in the Plate 2 caption.

An examination of root-mean-square values indicates the relative role of the various terms in the vertical momentum balance. These values are listed in Table 1. The values in Table 1 are computed using all values in the domain for the duration of the experiment. The values in Table 1 are consistent with the ratios seen in Plate 2 and indicate that the vertical acceleration is the largest contributor to the departure from the hydrostatic balance. Table 1 also indicates the relative role of the biharmonic smoothing function. During plume events, strong gradients exist in the momentum and salt fields and are locally largest around the perimeter of the sinking plumes. The biharmonic operator acts locally to smooth these gradients at the grid scale. The rms value of this term is $\sim 30\%$ of the vertical pressure gradient term.

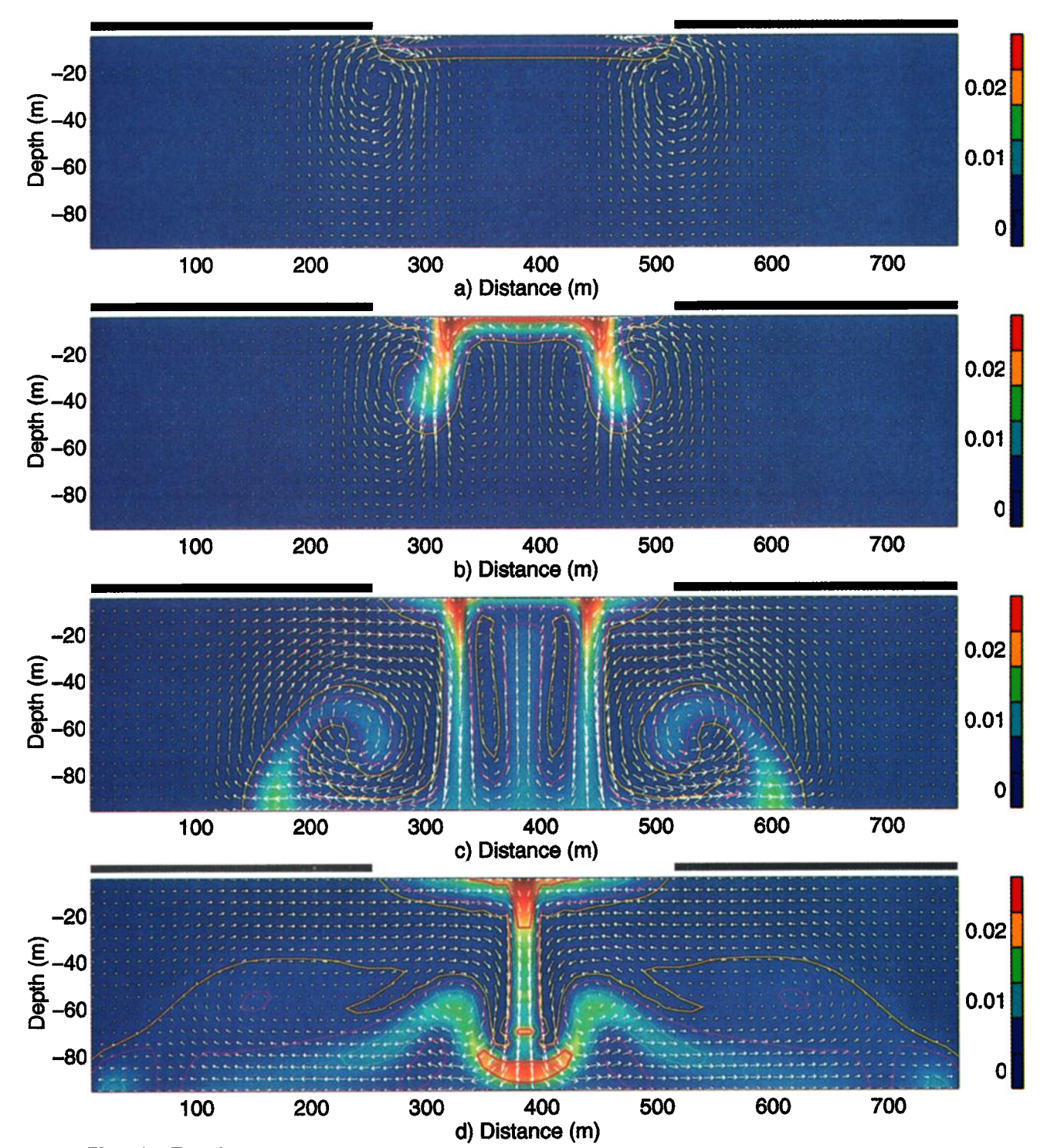


Plate 1. Experiment 1, stationary lead, homogeneous case (velocity and salinity distribution at t=1.5, 3, 4.5, and 6 hours). Lead boundaries are fixed at 250 and 500 m. In this and subsequent salinity figures, only the anomaly from 31.0 parts per thousand (ppt) is color shaded. The color range spans the values of salinity from 0.0025 to 0.03 ppt to emphasize the plume salinity, which has a maximum value of 0.03 ppt (red). Color contour values (0.0025, 0.005, 0.0075, and 0.01 ppt) are superimposed. Maximum vertical velocity in this simulation is 0.08 m s⁻¹.

This experiment illustrates that strong departure from the hydrostatic balance occurs during the vertical acceleration of plumes released in the lead. Root-mean-square values and spatial maps indicate that nonhydrostatic effects are order 1

terms in the momentum balance in the vicinity of the plumes. The inclusion of the Arctic halocline in the following experiment will significantly alter the proportionate role that nonhydrostatic effects play in the lead convection problem.

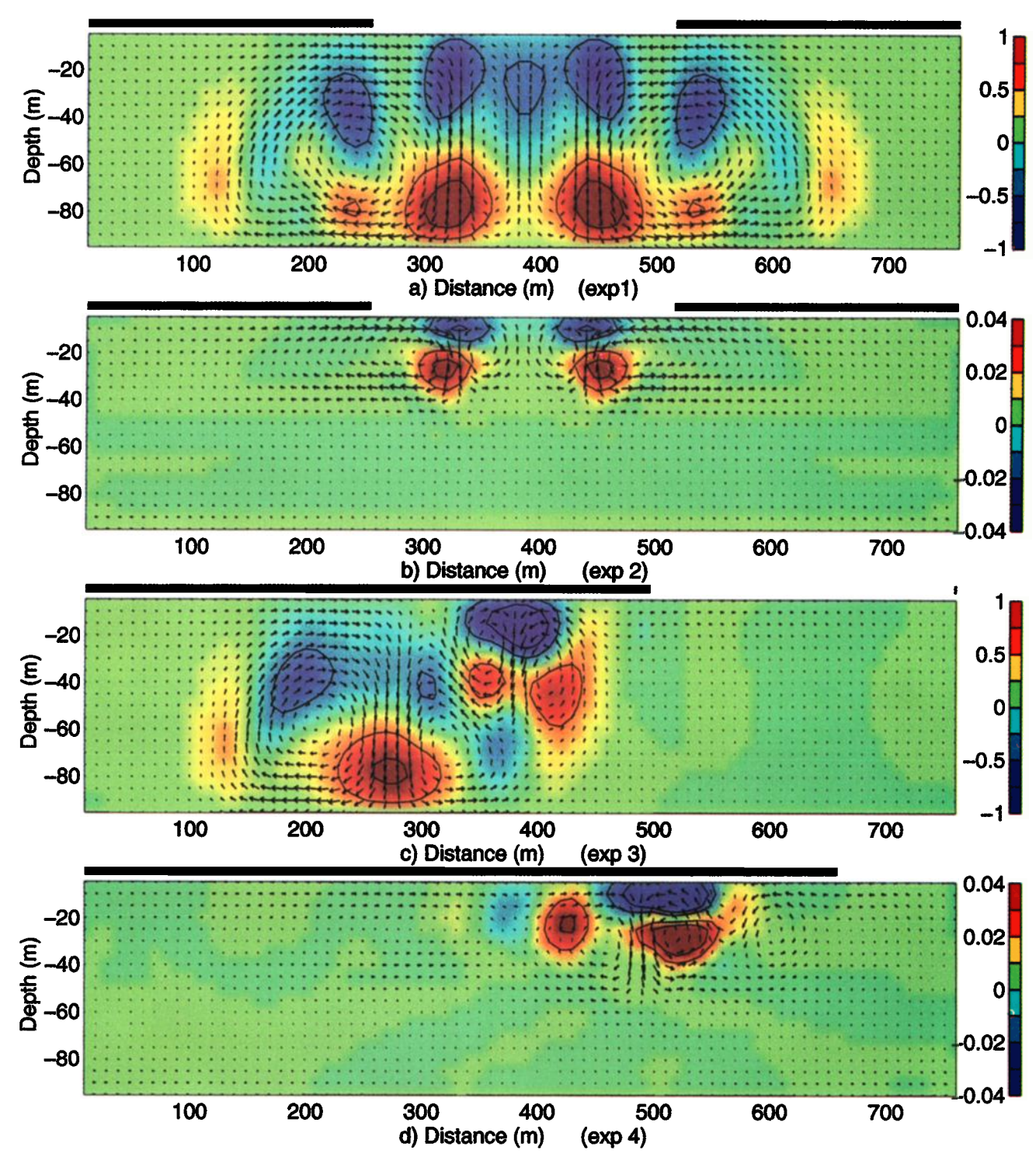


Plate 2. Experiments 1-4, distribution of NH_{Σ} t=4.5 hours (experiments 1-3) t=6.0 hours (experiment 4), NH_{Σ} is defined by (5) in the text and is nondimensional. For descending motion, maximum negative values of NH_{Σ} are near the surface, along the axes of descending plumes where fluid acceleration occurs, and maximum positive values are where fluid vertical deceleration occurs. Fluid vertical deceleration occurs near the bottom in homogeneous cases 1 and 3 and at the top of the halocline in stratified cases 2 and 4. For ascending motion, NH_{Σ} reaches a maximum value of only -0.05 in homogeneous experiments 1 and 3. (a) Experiment 1, stationary homogeneous case, t=4.5 hours. Contour values are (-2.0, -1.0, -0.5, 0.5, and 1.0). Maximum negative value (blue) is -0.9. Maximum positive value (red) is 0.9. (b) Experiment 2, stationary stratified case, t=4.5 hours. Contour values are (-0.04, -0.02, 0.02, and 0.04). Maximum negative value (blue) is -0.04. Maximum positive value (red) is 0.06. (c) Experiment 3, moving lead ($u_{\rm ice}=0.03~{\rm m~s}^{-1}$), homogeous, t=4.5 hours contour values are (-2.0, -1.0, -0.5, 0.5, 1.0, and 2.0). Maximum negative value (blue) is -1.7. Maximum positive value (red) is 1.09. (d) Experiment 4 moving lead ($u_{\rm ice}=0.03~{\rm m~s}^{-1}$) stratified, t=6.0 hours. Contour values are (-0.04, -0.02, 0.02, and 0.04). Maximum negative value (blue) is -0.1. Maximum positive value (red) is 0.07.

Experiment	w	∂w/∂t	u dw/dx	w∂w/∂z	$1/\rho_o \ \partial p'/\partial z$	ρ'/ρ _ο g	$B_H \nabla^4 w$
1	0.41E-2*	0.15E-4	0.27E-5	0.45E-5	0.20E-4	0.22E-4	0.71E-5
2	0.98E-3	0.27E-4	0.61E-6	0.12E-5	0.11E-3	0.11E-3	0.45E-5
3	0.35E-2	0.17E-4	0.28E-5	0.48E-5	0.22E-4	0.24E-4	0.76E-5
4	0.10E-2	0.29E-4	0.67E-6	0.11E-5	0.96E-4	0.95E-4	0.45E-5

Table 1. Root-Mean-Square Values of the Terms in the Vertical Momentum Equation

3.2. Stationary Lead, Halocline

In this experiment the lead is stationary, and a halocline represented by a linear increase in salinity from 31.0 parts per thousand (ppt) at z=-40 m to 31.2 ppt at z=-80 m is included in the initial condition. This stratification might represent a near-shore lead early in the freezing season. The Brunt-Vaisala frequency for this stratification is ~ 6 cph. Plate 3 shows the velocity and salinity field. Again, plumes are released initially at lead edges with subsequent inward migration. Maximum vertical velocities are, however, much weaker, reaching only 0.016 m s⁻¹.

In contrast to homogeneous experiment 1, where nonhydrostatic effects can be order 1 terms in the vertical momentum balance, these terms are relatively small in this experiment. Plate 2b shows the distribution of the nonhydrostatic terms (again as a ratio relative to the rms vertical pressure gradient). Maximum values do not exceed 5%, even during plume events. The presence of the halocline limits the vertical acceleration of the plumes. The rms values (Table 1) also support this reduced role of nonhydrostatic terms when the halocline is present. Again, the vertical acceleration dominates over nonlinear advection. Biharmonic smoothing reaches only 20% of the vertical acceleration term, indicating that nonhydrostatic effects are not being dominated by numerical dissipation.

3.3. Moving Lead, Homogeneous

Experiment 3 is a repeat of experiment 1 for a lead moving 3 cm s⁻¹ relative to the upper ocean. Plumes are released (Plate 4) at the trailing edge of the lead. This is consistent with the combined effect of stationary lead vorticity generation (discussed above) and vorticity generation associated with the moving lead. For a lead moving in the +x direction the icewater stress term τ_{iw} provides $+\zeta_y$ vorticity everywhere in the turbulent boundary later, except in the lead. This augments $+\zeta_y$ on the downstream (left) lead edge associated with lateral density variation there. Conversely, on the upstream (right) boundary, $+\zeta_y$ generated by τ_w counters $-\zeta_y$ associated with $-(\partial \rho/\partial x)$. These arguments assume that $(\partial \rho/\partial x)$ is largest at lead edges with small lateral variation in density within the lead. Spatial maps of $+\zeta_y$ are provided by *Smith and Morison* [1993] for the case of a moving lead in a hydrostatic model.

As in experiment 1, nonhydrostatic effects are order 1 contributors to the vertical momentum balance. A spatial map of these terms (Plate 2c) again indicates that these are largest along the axes of sinking plumes, with NH_{Σ} reaching values of -1.7. The rms values (Table 1) for experiment 3 are approximately the same as those for experiment 1. Again, however, the inclusion of the Arctic halocline at 40 m depth will limit the relative importance of these terms.

3.4. Moving Lead, Stratified

Plates 5 and 2d show salinity field and corresponding non-hydrostatic term maps for the moving lead ($u_{ice} = 0.03 \text{ m s}^{-1}$)

case over the halocline used in experiment 2. As in the moving lead, homogeneous case (experiment 2) plumes are shed downstream of the trailing lead edge. NH_{Σ} values are comparable to those seen in the corresponding stationary lead case. Nonhydrostatic effects are still less than a tenth of those associated with the hydrostatic balance. Root-mean-square values of the various nonhydrostatic terms (Table 1) are again comparable with the stationary case (experiment 2). The maximum value of NH_{Σ} reaches $\sim 8\%$, indicating the largely hydrostatic nature of the process.

In this and in the stationary case where stratification is present the plumes spread laterally across the top of the halocline. There is no evidence that the plumes can penetrate the existing stratification. As discussed by S. Narimousa and T. Maxworthy (unpublished manuscript, 1994), the ability of convective events to penetrate an existing stratification depends on the buoyancy flux (q_0) at the surface, the width of the buoyancy source (R), the depth of the convective mixed layer (h_0) , and the buoyancy (g') of the stratified interface. These can be quantified in terms of a Richardson number, Ri, and a Rossby number, R_0^*

$$Ri = \frac{g'h_0}{(q_0R)^{2/3}} \tag{13}$$

$$R_0^* = \left(\frac{q_0}{t^3 h_0^2}\right)^{1/2} \tag{14}$$

On the basis of scale analysis and laboratory experiments with a rotating tank they find critical values of R_0^* and Ri for which convective events penetrate a density interface. Their results indicate that plumes are unable to penetrate a density interface when Ri > 12, independent of R_0^* . This Richardson number criterion is also found in the nonrotating laboratory experiments of Ching et al. [1993]. For our stratification, $g' = 0.01 \text{ m s}^{-2}$, $h_0 = 40 \text{ m}$, $q_0 = 2 \times 10^{-7} \text{ m}^2 \text{ s}^{-3}$, and R = 250 m. This gives a Richardson number of ~ 300 , greatly exceeding the value cited by S. Narimousa and T. Maxworthy (unpublished manuscript, 1994). Our Rossby number, $R_0^* \sim 7$, is near their highest experimental R_0^* value. Our results are therefore consistent with their laboratory findings.

3.5. Event Analysis

The rms values reported in Table 1 give a statistical view of the magnitude of nonhydrostatic effects in the vertical momentum balance. The spatial maps of NH_{Σ} (Plates 2a–2d) give an indication of the spatial distribution of these terms during a plume event. In this section we illustrate the differences between a hydrostatic and nonhydrostatic experiment in another manner. Plates 6a and 6b illustrate experiment 4 salinity (Plate 6a) and that in an equivalent hydrostatic simulation (Plate 6b) at the time of the main plume event (t=6.0 hours). The distributions are remarkably similar with nearly identical timing of plume release from the lead. The hydrostatic case has a

^{*}Read 0.41E-2 as 0.41×10^{-2} .

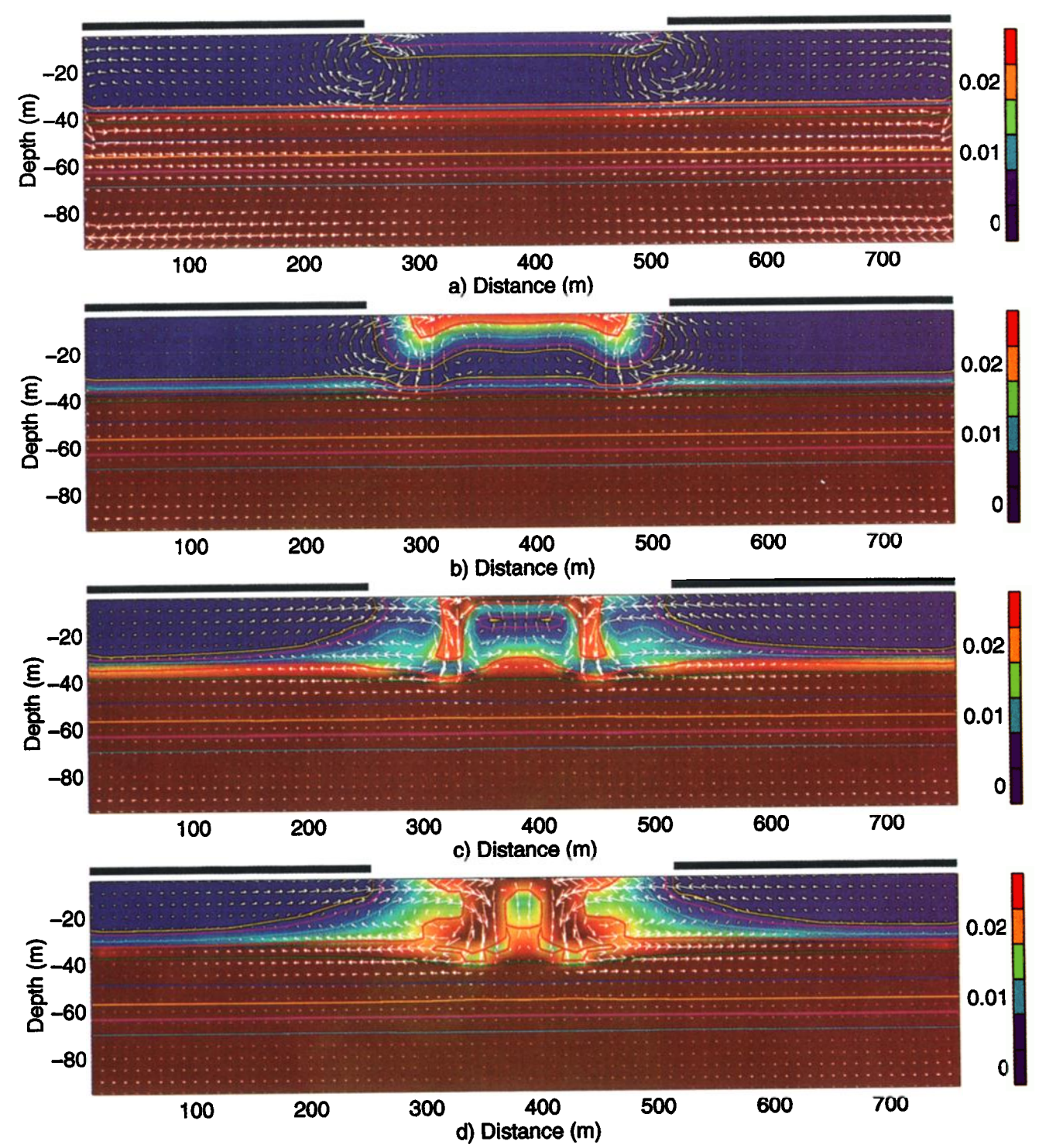


Plate 3. Experiment 2, stationary lead, halocline case (velocity and salinity distribution at t=(a) 1.5 hours, (b) 3 hours, (c) 4.5 hours, and (d) 6 hours). Lead boundaries are fixed at 250 and 500 m. The color shading is limited to the salinity range 0.0025 to 0.03 ppt as in Plate 1. Contour intervals are nonuniform to emphasize the salt anomaly of the plume relative to the background stratification. Contour values are (0.0025, 0.005, 0.0075, and 0.01 ppt) in the plume region and (0.2, 0.4, 0.6, 0.8, 1.0, and 1.2 ppt) for the halocline. Maximum vertical velocity in this simulation is 0.04 m s⁻¹. Maximum plume salinity anomaly is 0.03 ppt (red).

slightly stronger flow field with maximum vertical velocity reaching $-0.04~{\rm m~s^{-1}}$ versus $-0.03~{\rm m~s^{-1}}$ in the nonhydrostatic case.

As discussed above, Yang [1991] illustrated that nonhydrostatic effects translate into horizontal differences as well. Fol-

lowing Yang [1991], we examine lateral pressure gradients again at the time of the first plume event (t = 6.0 hours), which is the strongest during experiment 4. Plates 6c-6e show these pressure gradients obtained from the moving lead of experiment 4 ($u_{\rm loc} = 0.03$ m s⁻¹ with halocline). Plate 6c is the

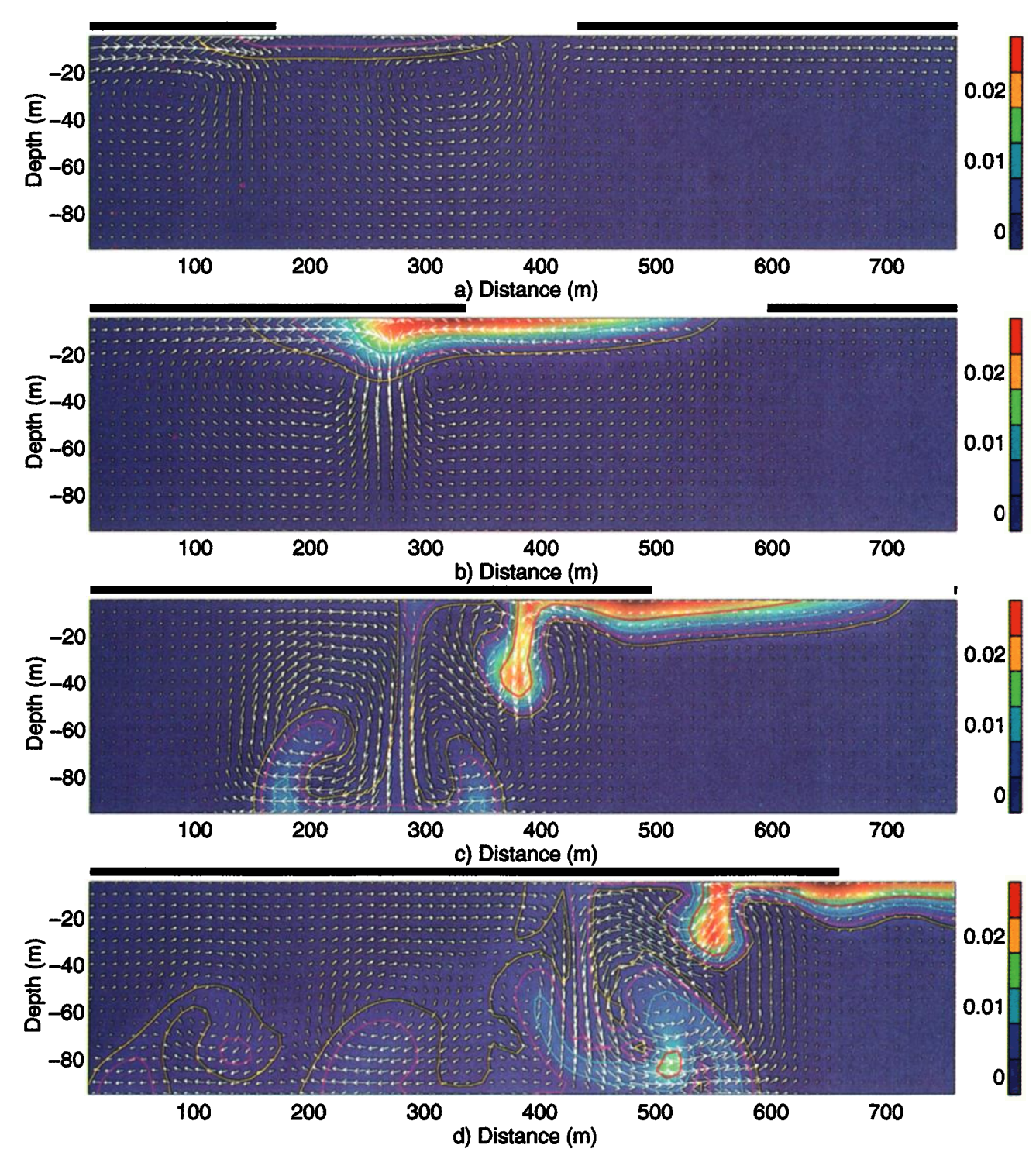


Plate 4. Experiment 3, moving lead ($u_{ice} = 0.03 \text{ m s}^{-1}$), homogeneous case (velocity and salinity distribution at t = (a) 1.5 hours, (b) 3 hours, (c) 4.5 hours, and (d) 6 hours). The trailing edge of the lead is located at 650 m at t = 6 hours. Color shading and contour values are as in Plate 1. Maximum vertical velocity in this simulation is 0.05 m s⁻¹. Maximum plume salinity anomaly is 0.03 ppt (red).

total pressure gradient field. Plate 6d is the hydrostatic component in nonhydrostatic experiment 4. Note that this is not the hydrostatic pressure obtained from the hydrostatic experiment shown in Plate 6b. The gradient fields are consistent with convergent motion at the surface and divergent motion at depth. A comparison of the total and hydrostatic pressure gradient fields indicates a qualitative similarity. Plates 6c-6e

are contoured relative to the magnitude of the average hydrostatic pressure gradient (= $1.0 \times 10^{-4} \,\mathrm{m \, s^{-2}}$) so that a relative comparison can be made. Maximum contour values in Plate 6d are thus O(1). The total pressure gradient (Plate 6c) maximum values only reach 50% of the hydrostatic pressure gradient. As Yang [1991] argued, hydrostatic pressure gradients and flow fields are stronger than nonhydrostatic ones. Plate 6e shows a

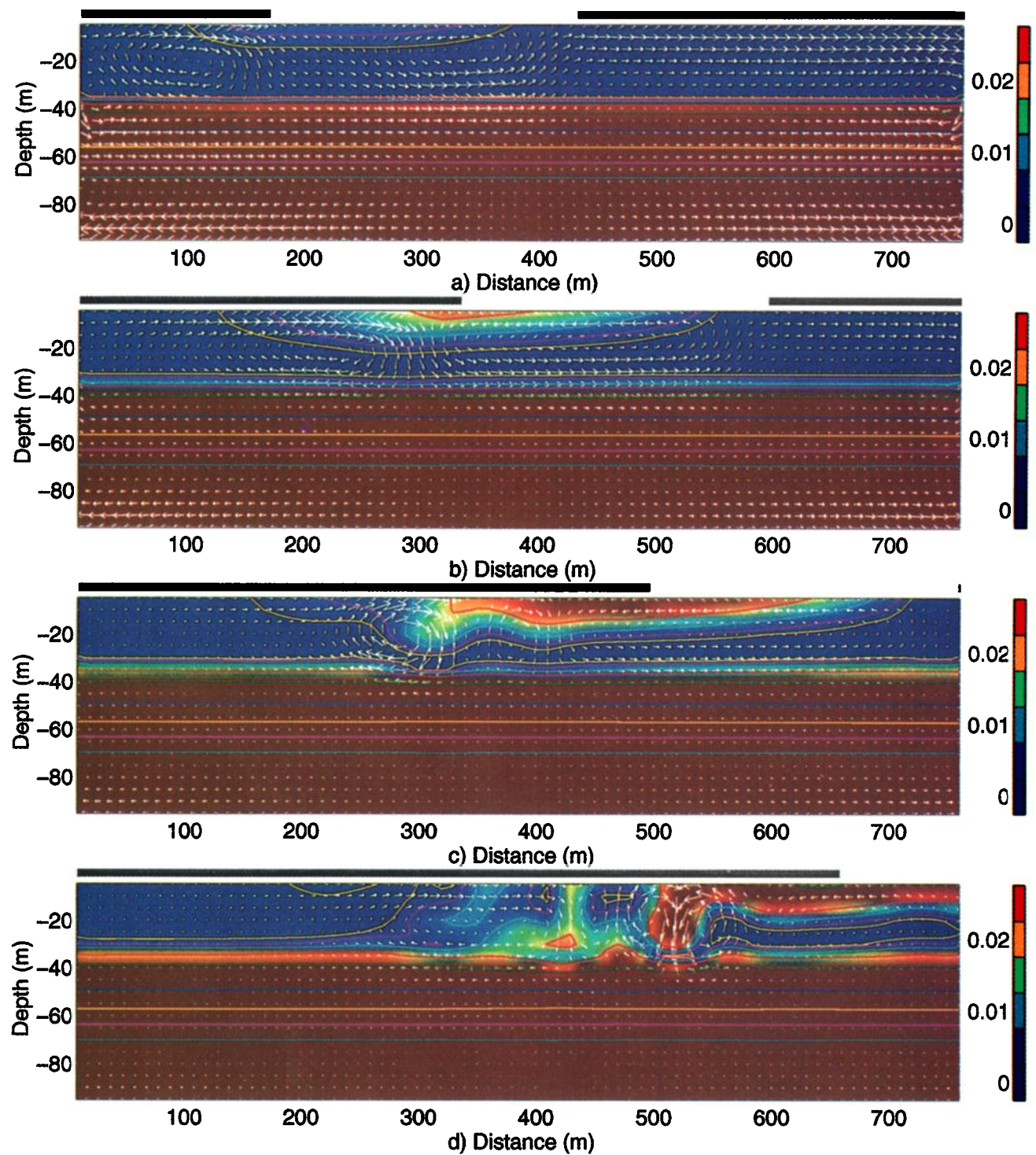


Plate 5. Experiment 4, moving lead ($u_{\text{ice}} = 0.03 \text{ m s}^{-1}$), halocline case (velocity and salinity distribution at t = (a) 1.5 hours, (b) 3 hours, (c) 4.5 hours, and (d) 6 hours). The trailing edge of the lead is located at 650 m at t = 6 hours. Color shading and contour values are as in Plate 3. Maximum plume salinity anomaly is 0.03 ppt (red). Maximum vertical velocity in this simulation is 0.03 m s⁻¹.

quantity Yang terms "nonhydrostatic residual pressure gradient." It is obtained by subtracting the hydrostatic pressure gradient from the total pressure gradient in the nonhydrostatic experiment. Plate 6e can be viewed as the difference field between Plates 6c and 6d. The nonhydrostatic residual pressure gradient field (Plate 6e) illustrates that maximum corrections to hydrostatic pressure gradients occur near the surface

only. Along the axes of sinking plumes, near the surface, the nonhydrostatic residual pressure gradient field (Plate 6e) is anticorrelated with the hydrostatic pressure gradient field (Plate 6d). Nonhydrostatic pressure gradients thus act to counter hydrostatic pressure gradients making the resulting nonhydrostatic flow cells weaker.

This residual pressure gradient field is thus similar to that

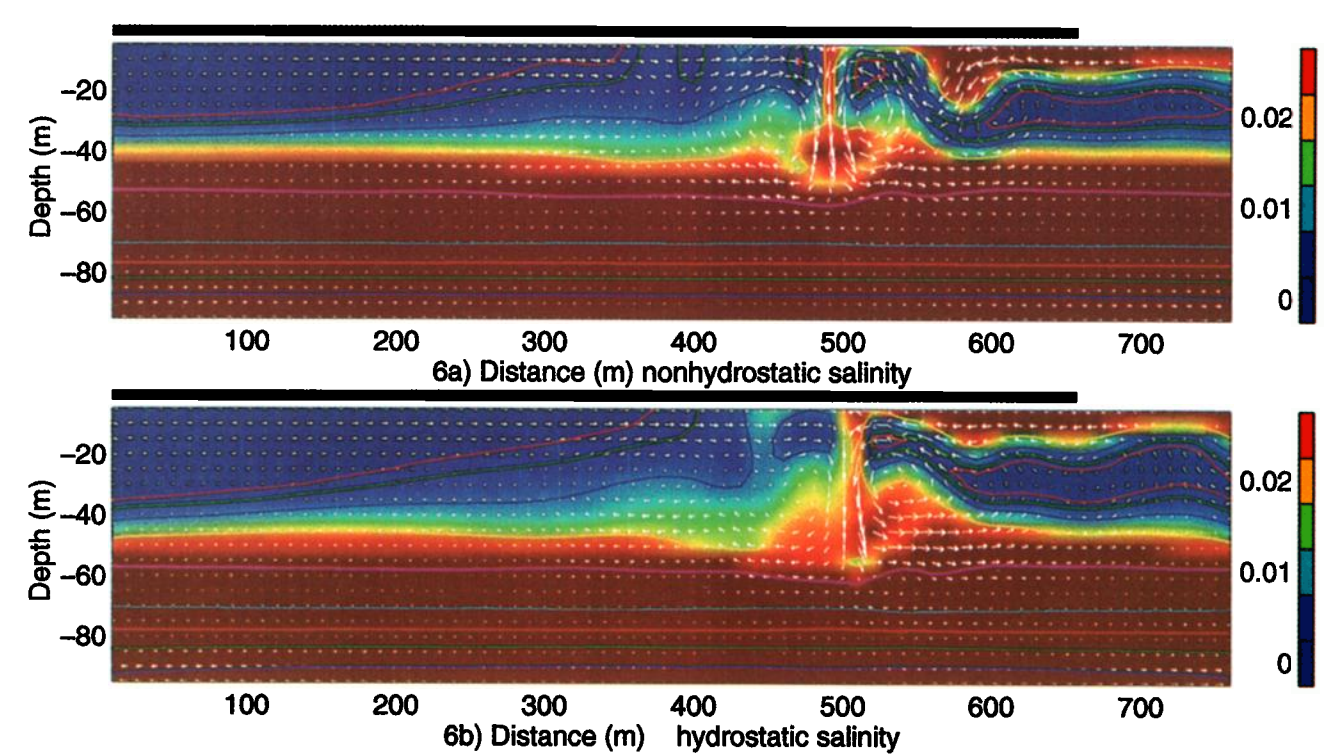


Plate 6. Event analysis (t=6.0 hours) experiment 4, moving lead ($u_{\rm ice}=0.03~{\rm m~s^{-1}}$), halocline case. (a) Salt distribution, nonhydrostatic case. Color shading and contour values are as in Plate 3. Maximum positive values are 0.03 ppt (red). (b) Salt distribution, hydrostatic case. Color shading and contour values are as in Plate 3. Maximum positive values are 0.03 ppt (red). (c) Lateral pressure gradient, nonhydrostatic case. Contour intervals are (-1.0, -0.5, -0.25, 0.25, 0.5, and 1.0). Maximum positive values are 0.5 (red), and maximum negative values are -0.5 (blue). (d) Lateral pressure gradient, hydrostatic case. Contour intervals are (-2.0, -1.0, -0.5, -0.25, 0.25, 0.5, and 1.0). Maximum positive values are 2 (red), and maximum negative values are -1 (blue). (e) Nonhydrostatic residual pressure gradient (c-d). Contour intervals are (-2.0, -1.0, -0.5, -0.25, 0.25, 0.5, 1.0, and 2.0). Maximum positive values are 1 (red), and maximum negative values are -2 (blue). The fields in Plates 6c-6e are contoured relative to the magnitude of the average hydrostatic pressure gradient ($=1 \times 10^{-4}~{\rm m~s^{-2}}$) so that a relative comparison can be made.

presented by Yang [1991]. Yang's nonhydrostatic residual pressure gradient field [Yang, 1991, Figure 6] shows a similar weakening tendency which decreases with distance from the buoyancy source.

A distinction between results here and those presented by Yang [1991] lies in model formulation. Yang's model explicitly carries a vertical turbulence term w'w' in the vertical momentum equation. The model then uses a turbulence parameterization (like Mellor and Yamada's [1982] turbulence scheme, 2.5) where the w'w' term is parameterized based on an atmospheric boundary layer model utilizing the Monin-Obukhov length. Yang found this nonhydrostatic term to be the dominant contributing term in the boundary layer, while the vertical acceleration term was important in the upper layers. It is important to note that our model does not incorporate this vertical turbulence term. We are thus unable to quantify the importance of this nonhydrostatic term in oceanic lead convection. However, on the basis of Yang's [1991, Table 2] results, it seems likely that this term would only be important very near the surface in the turbulent boundary layer.

4. Comparison With Rayleigh-Benard Theory

The convective flow between two rigid boundaries, subject to an adverse temperature gradient, is described by linear Rayleigh-Benard theory. *Chandrasekhar* [1961] summarizes many aspects of this problem. Steady state convection cells are established in this problem in response to the competing effects of buoyancy and molecular viscosity and diffusion. A critical Rayleigh number must be exceeded for the instability to occur. The Rayleigh number is defined

$$Ra = \frac{g\alpha_S \frac{\partial S}{\partial z} h^4}{k_T \nu} \tag{15}$$

where α_S is the saline coefficient of expansion (=8.0 × 10⁻⁴), k_T is thermal diffusivity coefficient, and ν is molecular viscosity. Here $\partial S/\partial z$ is a critical salinity gradient, and h is the distance between the boundaries. The critical value depends on boundary conditions but is generally of O(1000). Despite the fact that lead convection is not steady and the source of buoyancy is only at one boundary, some interesting comparisons can be made. A comparable analysis is made by *Jones and Marshall* [1993] in the context of deep convection in a coarser resolution nonhydrostatic numerical model.

We have evaluated the Rayleigh number for three experiments in which the buoyancy flux q_0 is varied about the central value ($q_0 = 2.0 \times 10^{-7} \text{ m}^2 \text{ s}^{-3}$) in the experiments above. The lead is stationary, and the fluid is initially homogeneous.

Figure 1 shows the maximum value of the Rayleigh number for experiments with $q_0 = 1.0 \times 10^{-7}$ (experiment 5), 2.0×10^{-7} (experiment 6), and 3.0×10^{-7} m² s⁻³ (experiment 7).

We evaluate a turbulent analog of the Rayleigh number as follows. Values of $(\partial S/\partial z)$ values are obtained from time series of maximum salinity gradient during the simulation. Preceding convective events, these reach maximum values of 0.5×10^{-3} , 1.5×10^{-3} , and 2.5×10^{-3} for the three experiments. The diffusion and viscous parameters k_T and ν are obtained from the turbulent biharmonic salinity diffusion coefficient B_S and momentum dissipation coefficients, A_S and A_H , we have run the model with Laplacian diffusion and dissipation. Experiments produce similar flow fields for

$$A_H = 1/4 \, \frac{B_H}{2\Lambda r^2} \tag{16}$$

$$A_S = 1/4 \frac{B_S}{2\Delta x^2} \tag{17}$$

We have found that these are more important in controlling the convective events than are the vertical diffusion terms represented by the *Pacanowski and Philander* [1981] scheme. The conclusion that lateral viscous effects dominate over vertical ones is also made by *Davey and Whitehead* [1981] in an analytic study of convection, with which we will make further comparisons below.

We have chosen a depth of 10 m for the value of h. Because we are forcing near one boundary only, taking h to be the depth of the fluid seems inappropriate. Instead, we identify hwith the near-surface conductive boundary layer. Maps of maximum $(\partial S/\partial z)$ indicate that the maximum gradient of salinity prior to convective events is contained in the upper several grid cells. In all experiments the first appearance of an unstable wave occurs at $\approx t = 3$ hours. All three curves in Figure 1 show an increase in Ra slightly before this time. This lags behind the spin-up time for q_0 , which reaches its maximum value in 1 hour. This suggests a diffusive timescale for the conductive boundary layer to adjust, reaching a maximum (∂S / ∂z) before becoming unstable. If we take $A_s = 0.01 \text{ m}^2 \text{ s}^{-1}$, the timescale for the boundary layer to thicken to 10 m is ≈3 hours. A number of laboratory studies have illustrated this diffusive growth of the unstable layer with subsequent release of unstable plumes. These include Howard [1964], Foster [1971], Foster and Waller [1985], and Fernando et al. [1991]. An important distinction between our experiments and those of Kantha [1995] exists and is related to this time dependent release of plumes from the boundary layer. Kantha's results indicate less time dependence in the lead cell circulations, which may be related to the Mellor and Yamada [1982] turbulence closure in that model. Because the LeadEx observations indicate a transient time dependent nature of the plume release we feel that this aspect of our model simulations is a realistic one.

Given these choices of parameters for the estimation of the Rayleigh number, the resulting values indicate that a critical Rayleigh number of $\approx \! 1000$ must be exceeded in order for instability to occur. The main peaks in Rayleigh number in Figure 1 coincide with plumes being released from the boundary layer. Hence higher buoyancy flux values produce greater growth rates and more frequent plumes.

In an analytic study of convection, *Davey and Whitehead* [1981] determined growth rates and wavenumber of the fastest

growing unstable wave in a two-layer system with rotation. They show that these depend on the density difference between the layers (expressed in terms of $g'=g\Delta\rho/\rho$), the layer thickness ratio (H_1/H_2) , and Laplacian lateral viscosity and diffusion coefficients $(A_H$ and $A_S)$. We estimate representative values of g' based on the maximum values of $(\partial S/\partial z)$ cited above. The values of A_H and A_S are those used above. On the basis of their expressions for growth rate

$$\sigma = 2^{-3/4} g'^{3/4} A_H^{-1/2} H^{1/4}$$
 (18)

and wavenumber K

$$K = 2^{-1/4} g'^{1/4} A_H^{-1/2} H^{-1/4}$$
 (19)

we estimate periods and wavelengths for the three experiments in which q_0 is varied 1.0×10^{-7} , 2.0×10^{-7} , and 3.0×10^{-7} m^2 s⁻³. These expressions indicate that the growth rate σ is more sensitive to g' than is the wavenumber of the fastest growing wave. Taking $H_1 = 10$ m, we estimate wavelengths $(L = 2\pi/K)$, which range 31-39 m and periods $(T = 2\pi/\sigma)$ ranging 1570-3280 s. In our experiments the fastest growing wave is typically ≈100 m, and the period in the three experiments shown in Figure 1 is 1-3 hours. While agreement is not exact, the results are of the same order of magnitude. Jones and Marshall [1993] also concluded that the initial plume scale in their model simulations of deep convection were in rough agreement with linear theory. The results are also in qualitative agreement with respect to the sensitivity of σ and K to g'. As noted above, the frequency of the plumes does increase with buoyancy flux after the initial spin-up as the results of Davey and Whitehead [1981] indicate. The wavelength of the fastest growing wave remains, however, ≈100 m in all experiments

These expressions for growth rate and wavelength neglect the effects of planetary rotation, f. Davey and Whitehead [1981] showed that the inclusion of rotation attenuates growth rates but only for wavelengths greater than the internal Rossby radius of deformation. Our wavelengths are much smaller than this scale.

5. Conclusions

We have examined nonhydrostatic effects in shallow convective circulations associated with leads in Arctic sea ice. The results indicate that these can be significant terms in the vertical momentum equation (Plates 2a and 2c) if the sinking plumes are free to accelerate to depths of 100 m or more. This may be the case in the eastern Arctic, where the halocline depth is relatively deep. In the vicinity of the LeadEx field experiment, however, the halocline depth is typically 30-40 m. In this case, numerical experiments indicate that nonhydrostatic effects are <10% in the vertical momentum equation (Plates 2b and 2d) and the vertical accelerations are limited spatially and temporally by the presence of the halocline. In addition to limiting nonhydrostatic effects in the fluid, the presence of the halocline serves to limit the depth of penetration of convective plumes. As found by S. Narimousa and T. Maxworthy (unpublished manuscript, 1994), a Richardson number scaling measures the strength of the buoyancy forcing relative to the strength of the stratification. For a Richardson number >≈12 they find that plumes cannot penetrate the stratification. Our results are in agreement with this finding suggesting that lead convection plumes are of insufficient

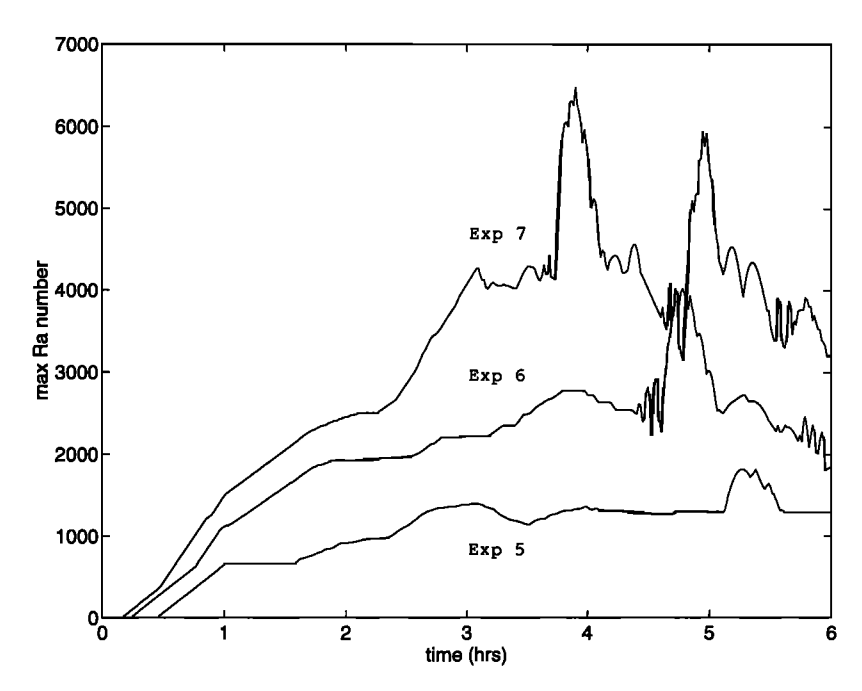


Figure 1. Experiments 5-7, time evolution of the maximum Rayleigh number, experiment 5 ($q_0 = 1 \times 10^{-7} \text{ m}^2 \text{ s}^{-3}$), experiment 6 ($q_0 = 2 \times 10^{-7} \text{ m}^2 \text{ s}^{-3}$) and experiment 7 ($q_0 = 3 \times 10^{-7} \text{ m}^2 \text{ s}^{-3}$).

buoyancy to penetrate the halocline. Instead, they spread laterally across the upper halocline as seen in model salinity distributions in Plates 3, 5, and 6a-6b.

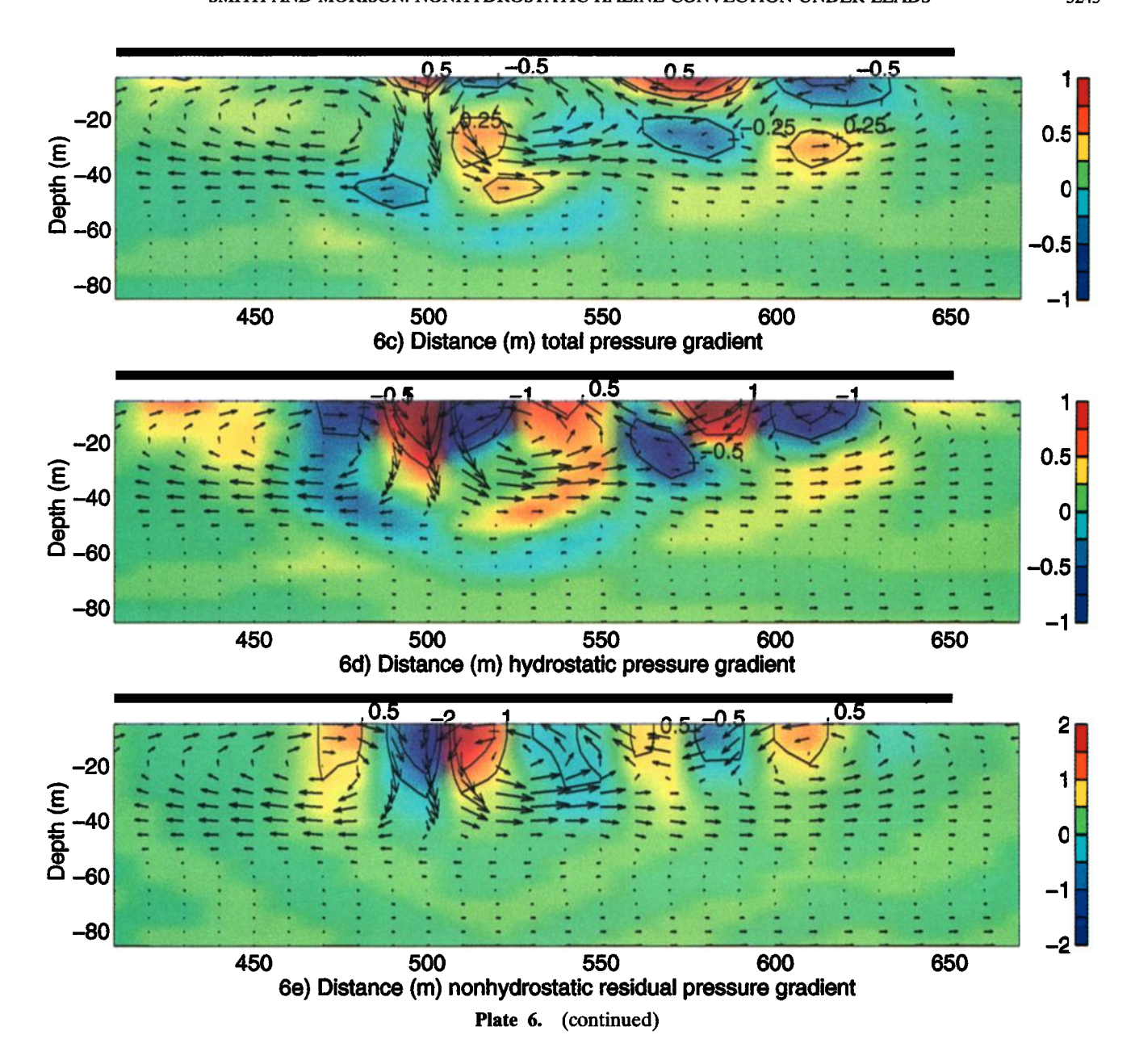
Nonhydrostatic effects also translate into lateral pressure gradients in the fluid. Spatial maps of these (Plates 6c-6e) indicate that these pressure gradients counter hydrostatic pressure gradients near the surface, making nonhydrostatic circulations weaker than hydrostatic ones. This result is in agreement with those found in a study of atmospheric convective circulations. Despite this weakening effect, the salt distributions in hydrostatic and nonhydrostatic simulations are remarkably similar.

Lead convection differs from traditional Rayleigh-Benard convection in a number of ways. The forcing is neither steady or stationary and occurs at one boundary only. In addition, the buoyancy forcing varies laterally along that boundary, associated with lead edges which trigger convective events. Despite these differences, we find that a critical Rayleigh number of O(1000) occurs before the onset of instability. Further, our results are in rough agreement with growth rate and wavelength predictions based on two-layer analytic solutions found by Davey and Whitehead [1981]. Our results support their conclusion that growth rate is more sensitive to buoyancy flux q_0 than is the wavelength of the instability. For a realistic range of lead q_0 values we find periods which range 1–3 hours for plume events but wavelengths of O(100 m) are found to be a robust scale in numerous experiments.

Observations made during LeadEx in 1992 are described by Morison and McPhee [this issue] and McPhee [this issue]. Here we briefly describe important similarities and differences between the model and experimental results. Perhaps the most important finding common to the modeling and observations is that for a slowly moving lead the salt rejected at the lead surface does not mix uniformly into the unstratified mixed layer. Instead, it sinks down to the base of the mixed layer and makes the mixed layer shallower and more stratified. This is

apparent in all the model results presented here. It is also indicated by the average horizontal profiles of salinity at lead 4 of LeadEx [Morison and McPhee, this issue, Figure 14a]. There the salinity in the middle of the mixed layer increased to a maximum at the downstream edge of the lead but decreased downstream of the lead. Downstream of the lead, the salinity in the middle of the mixed layer was not significantly greater than it was upstream. For this to happen, water near the surface passing under the lead from upstream must pass under the lead without increasing in salinity. This can occur in the model because the salinity plumes are intermittent as also observed at LeadEx. In nature the convection is also likely to be three dimensional, so upstream water can pass under the lead by going between plumes. The implications of plumes passing through to the mixed layer base are important in the context of parameterizing the upper ocean in large-scale models. If one uses a one-dimensional mixed layer model with the areal average buoyancy flux applied to the surface, the mixed layer will increase in salinity and deepen because of the instability of the boundary layer. This model and the experimental results imply that if the buoyancy flux is concentrated in narrow leads, the mixed layer actually responds in the opposite way, becoming more shallow and stratified. In large-scale, high-latitude ocean models it will be necessary to parameterize this effect of surface buoyancy flux differently depending on lead distribution, ice speed, and freezing rate. It may not be possible to use traditional one-dimensional mixed layer models for such situ-

One element of the model results that is surprising is how far the fully developed plumes may lag behind a moving lead. The LeadEx data showed significant velocity and some salinity disturbance downstream of the lead, but the strongest salt flux occurred close to the downstream edge. This may relate to the Rayleigh number and event timing described above. The more rapid cycling predicted by *Davey and Whitehead* [1981] should give less of a lag. However, the experimental results indicate



virtually no lag behind the trailing edge. As suggested by Morison and McPhee [this issue], flow disturbance and ice deformation at the ice floe edges may act as triggering mechanisms that enhance plume separation at the downstream edge. For example, the flow down and under the ice at the downstream edge imparts a downward vertical velocity at the edge that may trigger plumes there.

To explore how plume release timing and mechanical forcing at the downstream edge of the lead aid in fixing plumes to the lead edge (as opposed to trailing behind), we have conducted one final simulation. Two factors were changed in this experiment: reduced biharmonic dissipation and a downward body force in the vertical momentum equation, which moves with the downstream lead edge. Experiments 1–7 presented above were performed with a common value of the biharmonic dissipation coefficient B_H that allowed all simulations to be numerically stable. In this final simulation with stratification (a repeat of experiment 4) it has been possible to reduce B_H by a

factor of 4. In a simulation without the body force this alone allowed the trailing plumes to move closer to the lead edge but still trail behind by 100 m.

By continuity we expect a downward velocity of the order of the ice velocity in a narrow region in front of the downstream lead edge. Therefore we added a body force to the vertical momentum equation that produced a 0.03 m s⁻¹ downward vertical velocity at the downstream edge of the lead.

Plate 7 shows the results of these modifications. With the inclusion of the body force, plumes are now tied to the trailing edge in a manner which is more consistent with the observations. Plate 7 shows that the effective salt flux into the upper water column is increased. Maximum vertical velocity has increased to 0.05 m s⁻¹. The frequency of the plume events has increased consistent with (18). We thus conclude that mechanical forcing by the presence of the ice edge at the downstream lead edge is an important factor in controlling the pattern of lead convection.

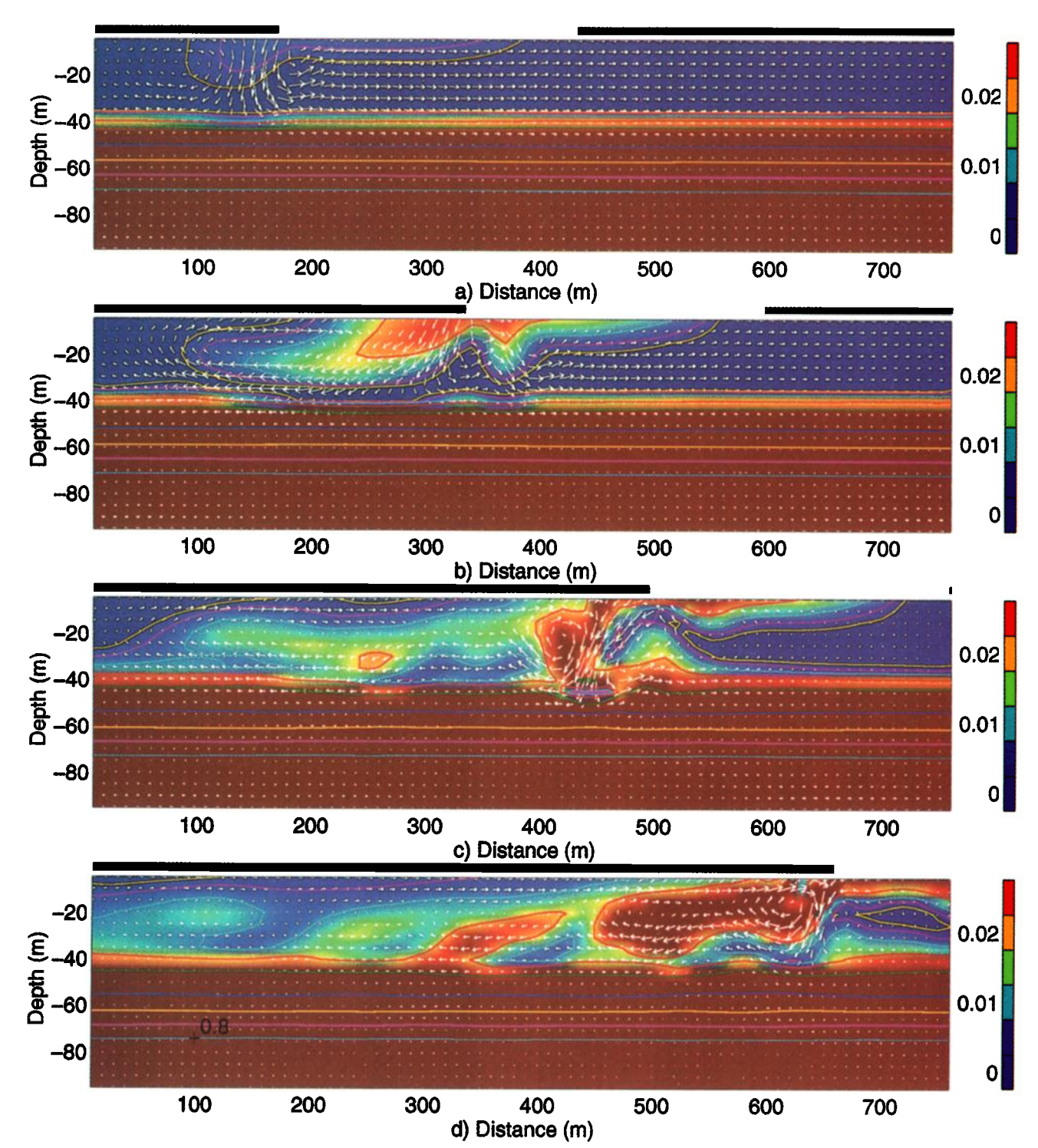


Plate 7. Experiment 8, moving lead $(u_{\text{ice}} = .03 \text{ m s}^{-1})$, halocline case with mechanical forcing at the downstream ice edge (velocity and salinity distribution at t = (a) 1.5 hours, (b) 3 hours, (c) 4.5 hours, and (d) 6 hours). The trailing edge of the lead is located at 650 m at t = 6 hours. Color shading and contour values are as in Plate 3. Maximum plume salinity anomaly is 0.03 ppt (red). Maximum vertical velocity in this simulation is 0.05 m s⁻¹.

Notation

- α_S saline expansion coefficient, equal to 0.8×10^{-4} .
- B_H biharmonic viscosity coefficient, equal to 0.4×10^2 m⁴ s⁻¹ (lateral) and 0.1×10^2 m⁴ s⁻¹ (vertical).
- B_S biharmonic salinity diffusion coefficient, equal to $0.2 \times 10^1 \text{ m}^4 \text{ s}^{-1}$ (lateral) and $0.05 \times 10^1 \text{ m}^4 \text{ s}^{-1}$ (vertical).
- C_{iw} ice-water drag coefficient, equal to 7.5×10^{-3} .
- $2\Delta t$ finite difference time step, equal to 2 s.

- $2\Delta x$ finite difference lateral grid cell resolution, equal to 10 m.
- $2\Delta z$ finite difference vertical grid cell resolution, equal to 5 m.
- F_S salt flux, equal to 2.0×10^{-5} kg m⁻² s⁻¹.
- Coriolis parameter, equal to 2Ω .
- gravitational acceleration.
- reduced gravity, equal to 0.01 m s⁻².
- domain depth, equal to 100 m.
- k_{τ} thermal diffusivity.
- vertical momentum diffusion coefficient [Pacanowski and Philander, 1981].
- k_s vertical salinity diffusion coefficient [Pacanowski and Philander, 1981].
- L_0 lead number [Morison et al., 1992], equal to $gMF_S d/\rho_0 u_{ice} u_*^2$.
- ν kinematic viscosity.
- $(\partial \rho/\partial S) = 0.808.$
- Brunt-Vaisala frequency, equal to $-g/\rho \ \partial \rho/\partial z =$ $1.0 \times 10^{-4} \text{ s}^{-1}$.
- NH_{Σ} $(\partial w/\partial t + u \partial w/\partial x + w \partial w/\partial z)/1/\rho_o \partial \rho'/\partial z$.
 - rotation rate, equal to 7.3×10^{-5} s⁻¹.
 - pressure.
 - Q_S source term for salt.
 - buoyancy flux, equal to $g/\rho F_S M = 1.7 \times 10^{-7}$ $m^2 s^{-3}$.
 - density of water.
 - Ra Rayleigh number.
 - Ri Richardson number.
 - R_0^* Rossby number.
 - S salinity.
 - ice water stress, equal to $\rho C_{iw}(u_{ice} u_{ocn})|u_{ice}$ τ_{iw} $-u_{\rm ocn}|$.
- u, υ, w velocity components in the x, y, and z directions.
 - friction velocity, equal to $C_{iw}^{1/2}u_{ice}$.
 - ice velocity, equal to 0.03 m s⁻¹
 - y component (along lead) of vorticity.

Acknowledgments. Computations were performed at UCSC with resources provided by G. K. Vallis. The research was sponsored by the Office of Naval Research, Arctic Programs under contract number N00014-92-J-1262 and by NASA contract NAGW 4213. Many discussions with colleagues have been an important part of this study. Those with J. W. Lavelle and R. D. Muench have been particularly useful.

References

- Brugge, R., H. L. Jones, and J. C. Marshall, Nonhydrostatic ocean modeling studies of open-ocean convection, in Deep Convection and Deep Water Formation in the Oceans, edited by P. C. Chu and J. C. Gascard, pp. 325-340, Elsevier, New York, 1991.
- Chandrasekhar, S., Hydrodynamic and Hydromagnetic Stability, Clarendon, Oxford, England, 1961.
- Ching, C. Y., H. J. S. Fernando, and Y. Noh, Interaction of a negatively buoyant line plume with a density interface, Dyn. Atmos. Oceans, 19, 367-388, 1993.
- Davey, M. K., and J. A. Whitehead, Rotating Rayleigh-Taylor insta-

- bility as a model of sinking events in the ocean, Geophys. Astrophys.
- Fluid Dyn., 17, 237-253, 1981. Fernando, H. J. S., and C. Y. Ching, Effects of background rotation on turbulent line plumes, J. Phys. Oceanogr., 23, 2125-2129, 1993a.
- Fernando, H. J. S., and C. Y. Ching, Lead induced convection: A laboratory perspective, J. Mar. Syst., 4, 217-330, 1993b.
- Fernando, H. J. S., R. R. Chen, and D. L. Boyer, Effects of rotation on convective turbulence, J. Fluid Mech., 228, 513-547, 1991.
- Foster, T. D., Intermittent convection, Geophys. Fluid. Dyn., 2, 201-217, 1971.
- Foster, T. D., and S. Waller, Experiments on convection at very high Rayleigh numbers, Phys. Fluids, 28, 455-461, 1985.
- Howard, L. N., Convection at high Rayleigh number, Appl. Mech. Proc. Int. Congr., 11th, 405-432, 1964.
- Jones, H., and J. Marshall, Convection with rotation in a neutral ocean: A study of open ocean deep convection, J. Phys. Oceanogr., 23, 1009-1039, 1993.
- Kantha, L. H., A numerical model of Arctic leads, J. Geophys. Res., 100, 4653-4672, 1995.
- Kozo, T. L., Initial model results for Arctic mixed layer circulation beneath a refreezing lead, J. Geophys. Res., 88, 2926-2934, 1983.
- Lavelle, J. W., and D. C. Smith IV, Effects of rotation on convective plumes from line segment sources, J. Phys. Oceanogr., 26, 863-872,
- Maxworthy, T., and S. Narimousa, Unsteady, turbulent convection into a homogeneous, rotating fluid with oceanographic applications, J. Phys. Oceanogr., 24, 865-887, 1994.
- McPhee, M. G., An inertial-dissipation method for estimating turbulent flux in buoyancy-driven, convective boundary layers, J. Geophys. Res., this issue.
- Mellor, G., and T. Yamada, Development of a turbulent closure model for geophysical fluid problems, Rev. Geophys., 20, 851-875, 1982.
- Morison, J. H., Forced internal waves in the Arctic, Ph.D. thesis, Univ. of Wash., Seattle, 1980.
- Morison, J. H., and M. G. McPhee, Lead convection measured with an autonomous underwater vehicle, J. Geophys. Res., this issue.
- Morison, J. H., M. G. McPhee, T. B. Curtin, and C. A. Paulson, The oceanography of winter leads, J. Geophys. Res., 97, 11,199-11,218,
- Pacanowski, R. C., and S. G. H. Philander, Parameterization of vertical mixing in numerical models of tropical oceans, J. Phys. Oceanogr., *11*, 1443–1451, 1981.
- Smagorinsky, J., General circulation experiments with primitive equations, I, Mon. Weather Rev., 91, 99-152, 1963.
- Smith, D. C., IV, and J. H. Morison, A numerical study of haline convection beneath leads in sea ice, J. Geophys. Res., 98, 10,069-10,087, 1993.
- Swarztrauber, P., and R. Sweet, Efficient FORTRAN programs for the solution of elliptic partial differential equations, NCAR Tech Rep. LA-109, Natl. Cent. for Atmos. Res., Boulder, Colo., 1975
- Xu, W., and C. A. Lin, A numerical solution of the linear Rayleigh-Benard convection equations with the B- and C-grid formulations, Tellus, Ser. A, 45, 193-200, 1993.
- Yang, X., A study of nonhydrostatic effects in idealized sea breeze systems, Boundary Layer Meteorol., 54, 183-208, 1991.
- J. H. Morison, Polar Science Center, Applied Physics Laboratory, University of Washington, 1013 NE 40th Street, Seattle, WA 98105. (e-mail: morison@apl.washington.edu)
- D. C. Smith IV, Environmental Fluid Dynamics Program, College of Engineering and Applied Sciences, Arizona State University, Tempe, AZ 85287-9809. (e-mail:dcsiv@asu.edu)

(Received August 17, 1994; revised June 2, 1997; accepted June 10, 1997.)